Dual electronic effects achieving a high-performance Ni(II) pincer catalyst for CO₂ photoreduction in a noble-metal-free system

Hai-Hua Huang[a,b] , Ji-Hong Zhang[c], Miao Dai[a,b], Lianglin Liu[a,b], Zongren Ye[a,b], Jiahao Liu[a,b], Di-Chang Zhong[c], Jia-Wei Wang[a,b] , Cunyuan Zhao[a,b], and Zhuofeng Ke[a,b,1]

A carbazolide-*bis*(NHC) Ni^{II} catalyst (**1**; NHC, *N*-heterocyclic carbene) for selective CO₂ photoreduction was designed herein by a one-stone-two-birds strategy. The extended π-conjugation and the strong σ/π electron-donation characteristics (two birds) of the carbazolide fragment (one stone) lead to significantly enhanced activity for photoreduction of CO₂ to CO. The turnover number (TON) and turnover frequency (TOF) of **1** were ninefold and eightfold higher than those of the reported pyridinol-*bis*(NHC) Ni^{II} complex at the same catalyst concentration using an identical Ir photosensitizer, respectively, with a selectivity of ∼100%. More importantly, an organic dye was applied to displace the Ir photosensitizer to develop a noble-metal-free photocatalytic system, which maintained excellent performance and obtained an outstanding quantum yield of 11.2%. Detailed investigations combining experimental and computational studies revealed the catalytic mechanism, which highlights the potential of the one-stone-two-birds effect.

carbazolide | photocatalytic CO₂ reduction | molecular catalysis | electron donation | extended conjugation

Photoreduction of CO₂ into synthetic fuels or fuel precursors is an attractive approach for global warming and energy shortage (1–3). A typical photocatalytic CO₂-reduction system contains a catalyst, a photosensitizer (PS), and a sacrificial donor. To date, noble-metal-based [Ru (4–6),Re (7–12), Ir (5, 13–15), etc.] complexes have been widely studied in CO₂ photoreduction as catalysts and/or PSs, whose applications were limited by the high costs. Some photocatalytic CO₂-reduction systems containing earth-abundant-metal-based PSs and catalysts (16–19) have been developed recently. Notably, organic dyes (20–28) are more intriguing for large-scale productions, owing to their high accessibility, low toxicity, and low cost (29). However, the performances for the CO₂ photoreduction systems with an organic PS and a non-noble-metal-based catalyst remain to be improved (20–23).

Structure-modification strategy is widely applied to the upgradation of the heterogeneous catalysts (30–34), as well as the homogeneous/molecular catalysts (13, 35–37). Rational modification on the ligand structure is a promising method to develop new molecular catalysts with higher catalytic rates, selectivities, and longevity, via intramolecular hydrogen-bond interaction (35), *trans* effect (36, 38, 39), and so on. According to the previous studies, strengthening the π-system of the catalyst (40–42) and enhancing the electron-donor ability of the ligand (13, 16, 37, 43) are two reliable strategies for the design of CO₂-reduction catalysts (Fig. 1). On one hand, the extended π-conjugation can stabilize some key intermediates by electron delocalization. Chang and coworkers (40) reported that the catalytic activities can be effectively improved by expanding the π-conjugated systems of the tetradentate *N*-heterocyclic carbene (NHC)–pyridine complexes at the appropriate position. Welch and coworkers (42) incorporated thienyl to replace phenyls as smaller heterocycles into the classic Fe–porphyrin catalysts, and the π-conjugation system was effectively extended compared with the out-of-plane phenyl-derived complex, leading to significantly enhanced performance. On the other hand, the stronger electron donor facilitates the activation of CO₂ as well as the C–O cleavage, which is usually considered as the rate-limiting step for CO formation. Webster, Delcamp, Papish, and coworkers (13) revealed a surprising effect from a remote O⁻ group on a pincer nickel complex, resulting in dramatically enhanced activity, which would be introduced in detail later. Royo, Lloret-Fillol, and coworkers (37) used the strong σ-donor NHCs to replace the bipyridine ligand of the classic Mn–carbonyl catalysts, and a clearly higher turnover frequency (TOF) was obtained. Inspired by these studies, we are motivated to simultaneously apply these two strategies on one CO₂-reduction

Significance

Light-driven CO₂ reduction into chemical fuels is intriguing for a sustainable carbon economy and global warming. However, the development of ideal CO₂-reduction catalysts remains a challenge. In this work, a one-stone-two-birds strategy was reported to improve the CO₂-reduction catalyst by introducing the carbazolide coordination site, which owns extended π-conjugation structure and strong electron-donating ability, achieving order-of-magnitude-enhanced performance. To our knowledge, the strategy of introducing a carbazolide coordination site has not been reported for the improvement of catalyst for CO₂ photoreduction. More importantly, a notable quantum yield of 11.2% was obtained with an organic photosensitizer, which is the highest value among the CO₂ photoreduction systems with a homogeneous organic photosensitizer and a non-noble-metal complex catalyst.
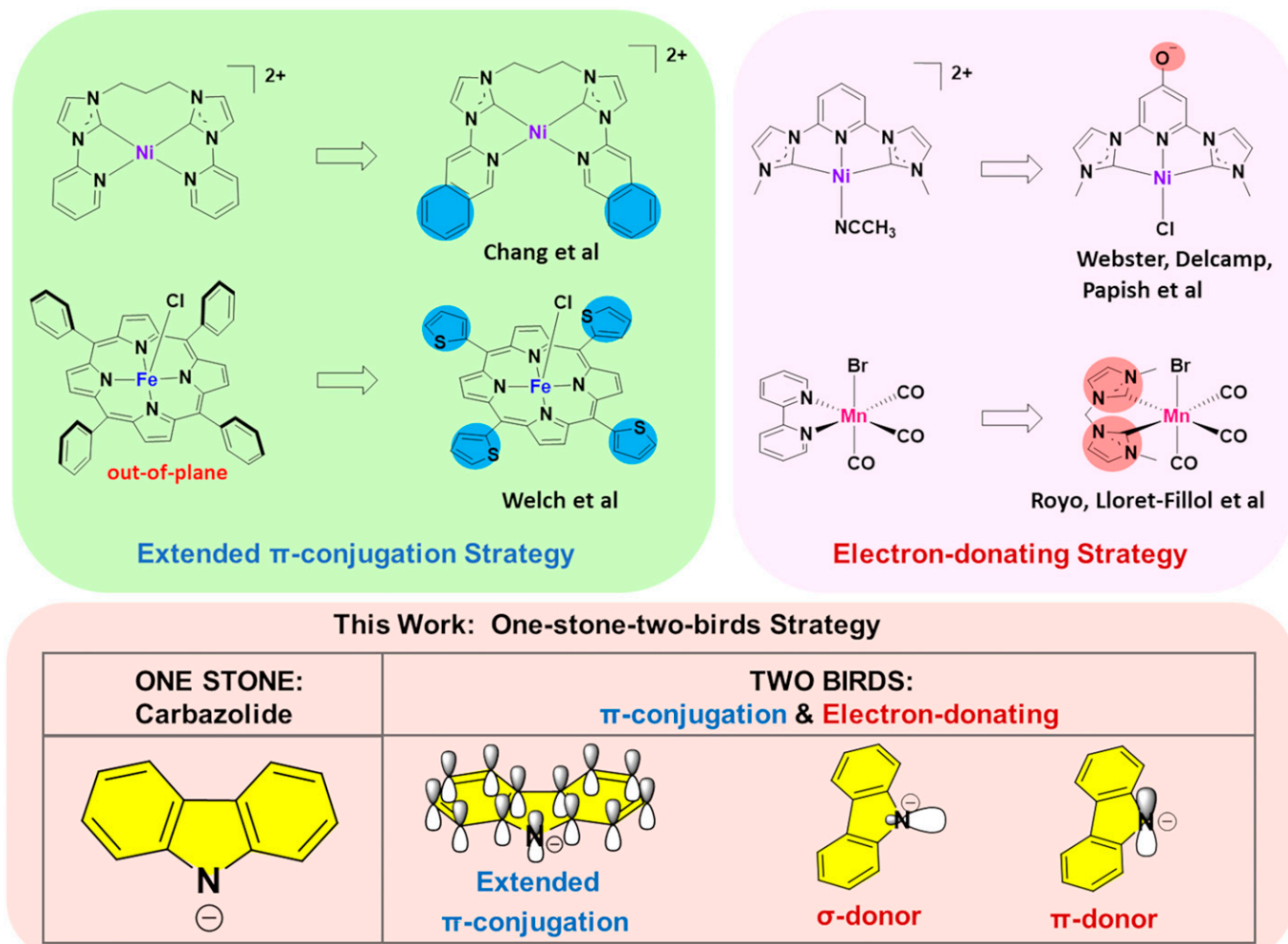
Fig. 1. Different strategies for the design of CO_2-reduction catalysts. Chang et al., ref. 40; Welch et al., ref. 42; Webster, Delcamp, Papish et al., ref. 13; Royo, Lloret-Fillol et al., ref. 37.

catalyst to achieve enhancing catalytic performance by the introduction of a strong electron donor with large π-conjugation. In this context, carbazolide attracts our interest due to its conjugative structure, as well as the strong electron-donor ability to the metal center through σ and π interactions (Fig. 1), which can be introduced into the ligand skeleton to achieve the one-stone-two-birds effect. Metal complexes comprising carbazolide-coordinating sites have been successfully applied to a variety of organic reactions (44–47), but haven't been reported as the catalysts in the area of CO_2 photoreduction as far as we know.

In this work, we chose to use a carbazolide-*bis*(NHC) pincer Ni^{II} complex, acetato[3,6-di-*tert*-butyl-1,8-*bis*(3-*n*-butyl-1-imidazolyl-2-ylidene)carbazolyl]nickel(II) (**1**; Fig. 2) as the catalyst in CO_2 photoreduction, whose single-crystal structure (47) was reported to exhibit a distorted square planar geometry (*SI Appendix,* Fig. S10) with bond angles of 162.90(12)° and 161.94(15)° for O(1)−Ni−N(1) and C(13)−Ni−C(20), respectively, consistent with the diamagnetic feature as suggested by the ^{1}H NMR (*SI Appendix,* Figs. S1 and S2). The coordination between the ligands and the Ni center was indicated by the bond length of 1.834(3) Å, 1.935(4) Å, 1.936(4) Å, and 1.902(2) Å for Ni–N(1), Ni–C(20), Ni–C(13), and Ni–O(1), respectively. NHC ligands have been widely used in the construction of CO_2-reduction catalysts owing to their strong σ-donating abilities (13, 37) and *trans* effect (36, 38, 39). Recently, nickel *bis*-NHC pincer complexes have attracted great attention for their high stabilities (48), as well as richer

interaction modes toward CO_2 molecule, compared to the traditional Ni^{II} complexes with tetradentate ligands, because CO_2 can access its two apical sites or the fourth equatorial site (49). In previous work, Webster, Delcamp, Papish, and coworkers (13) used a pyridinol-NHC pincer nickel complex to catalyze CO_2 reduction to CO in the presence of Ir(ppy)$_3$ (ppy, 2-phenylpyridine) and 1,3-dimethyl-2-phenyl-2,3-dihydro-1H-benzo[d]-imidazole (BIH), with a turnover number (TON) of 10.6, while the pyridine–NHC complex without a remote O$^-$ group exhibited negligible catalytic activity, indicating the key role of the electron-donor group. Nevertheless, the performances of the nickel *bis*-NHC pincer complexes remain to be further improved. Previous reports suggested that extended conjugation of some tetradentate nickel complexes comprising NHC moieties is beneficial for CO_2-reduction catalysis (40, 41, 50). Based on the above considerations, carbazolide moiety was introduced to extend the conjugation of the pincer *bis*-NHC complex, as well as donate electron density to the nickel center by σ and π interactions (**1**; Fig. 2), which may both benefit the catalytic activity. In addition, based on **1**, we have tried to construct a noble-metal-free photocatalytic system with an organic dye to replace the precious-metal-based PS.

Density functional theory (DFT) studies were carried out to obtain more theoretical foundations for our hypothesis (Fig. 2). Compared with the pyridinol, the carbazolide with an extended conjugation structure exhibits a lower lowest-unoccupied molecular orbital (LUMO) energy, which can potentially serve as an electron-transfer mediator to stabilize the key intermediates. On
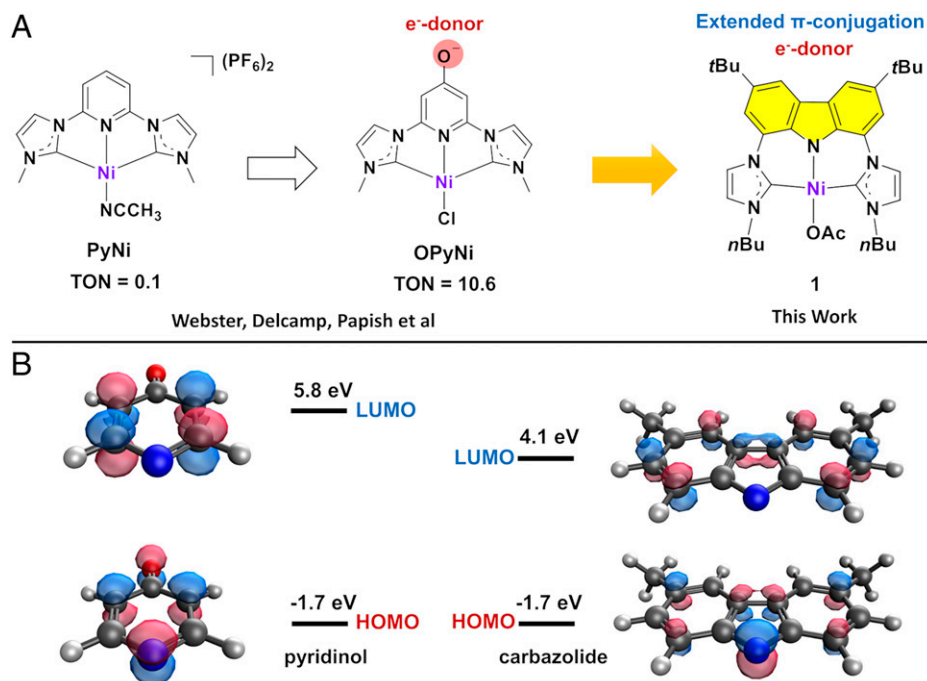
Fig. 2. Catalysts design. (*A*) Design of carbazolide-*bis*(NHC) pincer nickel catalyst for CO_2 reduction. Webster, Delcamp, Papish et al., ref. 13. (*B*) The HOMOs and LUMOs of the pyridinol and the carbazolide calculated at M06-2X (72)/def2SVP level of theory.

the other hand, the electron-donating ability of carbazolide is comparable with that of pyridinol, as indicated by the similar highest-occupied molecular orbital (HOMO) energy. Therefore, the carbazolide-based complex **1** designed by the one-stone-two-birds strategy is a potentially high-performance catalyst for CO_2 reduction.

Results

Electrochemical Characterization of 1. The electrochemical property of **1** was interrogated by cyclic voltammetry (CV) experiments. As shown in Fig. 3, **1** exhibits an irreversible reduction at -1.37 V vs. normal hydrogen electrode (NHE). The irreversibility of such a redox wave is probably due to the loss of the acetate anion accompanied by the reduction process, which will be discussed in detail later. This wave is probably corresponding to a 1-e$^-$ reduction process, as indicated by the diffusion-ordered spectroscopy and normal pulse-voltammetry results (*SI Appendix,* Figs. S11 and S12) (51). Under a CO_2 atmosphere, significant current enhancement can be observed in CV, suggesting the possible CO_2-reduction electrocatalysis that occurred at the Ni^I state. Although a well-defined catalytic peak is absent, **1** exhibits a less negative onset potential and, for the catalysis compared with that of the pyridinol–NHC pincer nickel complex (Fig. 3) reported in the literature (13), consistent with the extended π-conjugation of the carbozalide fragment with a lower LUMO energy (Fig. 2).

Photocatalytic CO_2 Reduction with Ir(ppy)$_3$. Since the electrochemistry results indicated that **1** is a potential catalyst for CO_2 electroreduction, we were activated to apply it into a photochemical CO_2-reduction system with the addition of a PS and a sacrificial donor, which can provide electrons during irradiation for the reduction of **1** and the further electron-transfer steps. In order to compare with the reported photocatalytic CO_2-reduction systems with other *bis*(NHC) pincer nickel complex catalysts, Ir(ppy)$_3$ was firstly chosen as the PS, which

possesses a large driving force (52) [-1.95 V vs. NHE for Ir(ppy)$_3$/Ir(ppy)$_3^-$] for the subsequent reduction of the catalyst (-1.37 V). BIH was used as a sacrificial donor because it is readily oxidized and is known to react with Ir(ppy)$_3$ during photolysis (5, 13, 50). In a 5-mL acetonitrile (MeCN) solution containing 0.1 mM **1**, 0.1 mM Ir(ppy)$_3$, 11 mM BIH, and 0.25 mL triethylamine (TEA) saturated with CO_2 (~0.28 M), 55.9 μmol of CO was produced with a negligible amount of H_2, giving a TON of 112 and the selectivity of ~100%, when irradiated by a 450-nm light-emitting diode (LED) light, with a light intensity of 100 mW·cm^{-2}, over a 3-h period (Fig. 4 and *SI Appendix,* Table S1). In order to make a comparison between **1** and the reported pyridinol-*bis*(NHC) Ni complex, chloro[4-oxido-2,6-*bis*(3-methyl-1-imidazolyl-2-ylidene)pyridinyl]nickel(II) (**OPyNi**),
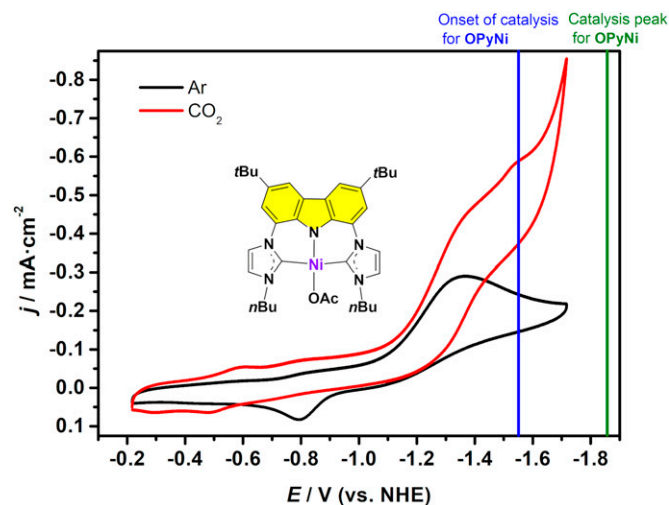

Fig. 3. Electrochemistry. CV of 1 mM **1** in CH$_3$CN solution containing 0.1 M TBAP under an Ar (black) or CO_2 atmosphere (red), by using a GC electrode with a scan rate of 100 mV·s^{-1}. The onset potential and the peak potential for the catalysis of **OPyNi** are shown by the blue line and green line for comparison, respectively (13).
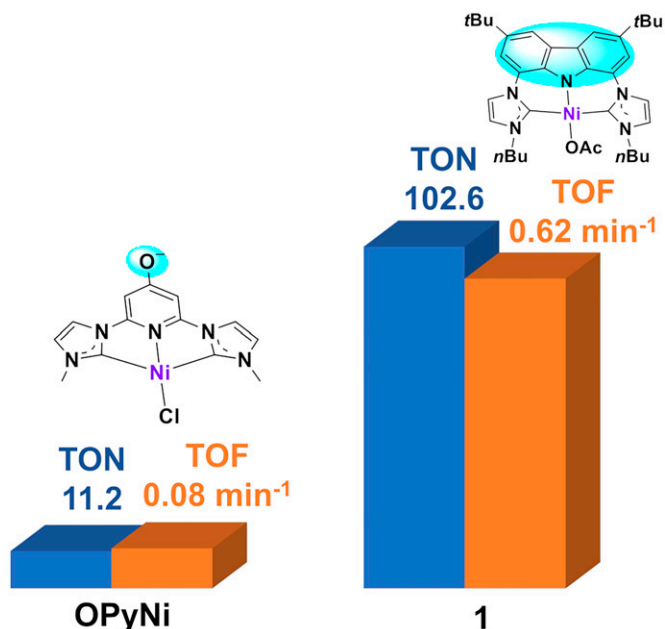
Fig. 4. The photocatalytic activities of **1** and **OPyNi** at identical conditions. Solutions were irradiated with a solar-simulated spectrum set to 1 Sun (300 W Xe lamp, AM 1.5 filter) for 4 h. Other conditions: 0.1 mM catalyst, 0.1 mM Ir(ppy)$_3$, 11 mM BIH, 0.25 mL of TEA, 1 atm of CO_2, and 5 mL of MeCN, room temperature.

the light source was changed to a xenon lamp with an air mass (AM) 1.5 filter for solar simulation (13), and both of these two complexes were tested under the same condition. Complex **1** exhibited higher performance by nearly 1 order of magnitude compared with **OPyNi** in terms of both TON (approximately ninefold, 102.6 vs. 11.2) for 4 h and TOF (approximately eightfold, 0.62 min^{-1} vs. 0.08 min^{-1}) for the first hour (*SI Appendix*, Fig. S16).

Photocatalytic CO_2 Reduction with Pheno. Since Ir(ppy)$_3$ is based on noble metal Ir, a cheap organic dye, 3,7-di([1,1′-biphenyl]-4-yl)-10-(naphthalen-1-yl)-10H-phenoxazine (**Pheno**; Fig. 5A), was chosen as the PS to replace Ir(ppy)$_3$, owing to its potentially large driving force (50, 53–56) (−1.80 V vs. saturated calomel electrode for **Pheno**$^+$/**Pheno*** in dimethyl acetamide) for the subsequent reduction of the catalyst (−1.37 V vs. NHE). The excellent catalytic performance was maintained when the PS was changed to **Pheno**. In a typical run, 21.4 μmol of CO was produced with no detected H$_2$ or HCOO$^-$, giving a TON of 143 and the selectivity of ∼100%, with a 3-mL acetonitrile solution containing 0.05 mM **1**, 0.1 mM **Pheno**, and 11 mM BIH, saturated with CO_2 (∼0.28 M) and tetraethylammonium bicarbonate (TEAB; ∼0.1 M, proton acceptor), irradiated by 425-nm LED light, with a light intensity of 100 mW·cm^{-2}, over a 2.5-h period (Fig. 5A and *SI Appendix*, Table S2). A TOF was obtained as 1.7 min^{-1} for an irradiation time of 15 min (*SI Appendix*, Fig. S28). When the catalyst concentration was increased to 0.1 mM, the TONs become 83 and 100 at BIH concentrations of 11 mM and 22 mM, respectively (*SI Appendix*, Table S2). A higher TON of 270 and TOF of 3.6 min^{-1} were obtained when [**1**] was decreased to 0.01 mM (Fig. 5B and *SI Appendix*, Table S2). The increased TON at low concentration can be ascribed to the relatively lower proportion of the catalyst molecules that participate in CO_2 reduction, while the remainder serves as the reservoir that is gradually deactivated during the catalysis (14, 21, 40), as indicated by the variation between the ultraviolet (UV)-visible (vis) spectra before

and after the photocatalysis (*SI Appendix*, Fig. S27). The TON can be further improved by the addition of BI$^+$ (N,N'-dimethyl-2-phenyl-benzo[d]imidazolium iodide), probably due to the weakened reduction power of the photocatalysis system, which diminishes the catalyst deactivation, although the driven force for catalysis is also weakened simultaneously. The highest TON of 393 was obtained at a [BI$^+$] of 22 mM (Fig. 5B and *SI Appendix*, Fig. S19).

According to the previous study, the addition of external Brønsted acid would facilitate the catalytic reduction of CO_2 to CO (35). A higher TOF of 2.7 min^{-1} was obtained by the addition of 2% water to the solution of the typical run, although the TON decreased to 86, probably due to the faster deactivation of the catalyst under a more acidic environment (*SI Appendix*, Fig. S18 and Table S2). A photochemical experiment with a lower light strength gave a TON of 101 for the water-containing system (*SI Appendix*, Fig. S29) and quantum yields of 11.2% and 11.1% were obtained for the initial 1 h and 1.5 h, respectively, which are higher than those of the reported photocatalytic CO_2-reduction systems with an earth-abundance-metal complex catalyst and a homogeneous organic PS, to the best of our knowledge (*SI Appendix*, Table S3) (21–23).

In order to investigate the necessity of each molecular component in such a photocatalysis system, several control experiments were carried out (Fig. 5A and *SI Appendix*, Table S2). First, no CO product was detected in an illuminated acetonitrile solution
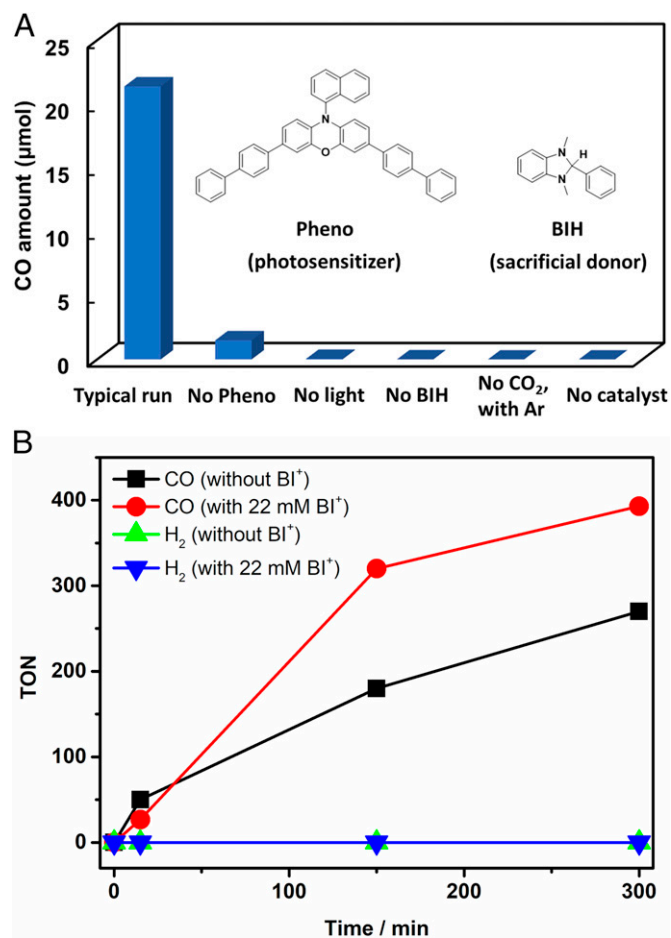
Fig. 5. (*A*) Control experiments catalyzed by **1** with **Pheno**. A typical run: 0.05 mM **1**, 0.1 mM **Pheno**, 11 mM BIH, saturated TEAB and CO_2, 3 mL of acetonitrile, room temperature, 425-nm LED light. Reaction time: 2.5 h. (*B*) Time profiles of photocatalytic CO and H$_2$ formation at a catalyst concentration of 0.01 mM with or without the addition of 22 mM BI$^+$. Other conditions: 0.1 mM **Pheno**, 11 mM BIH, saturated TEAB and CO_2, 3 mL of acetonitrile, room temperature, 425 nm LED light. Reaction time: 5 h.

with **Pheno** and BIH saturated with CO_2 in the absence of catalyst **1**. Control experiments without CO_2 also showed no CO generation under photochemical irradiation. When **Pheno** was removed, the amount of CO production dramatically reduced to 1.5 μmol from 21.4 μmol, indicating the vital role of the PS for the photocatalysis. Only a trace amount of CO was detected in the dark, which revealed the necessity of light for the photocatalysis. The absence of BIH also led to a negligible amount of CO. Moreover, the addition of Hg(0) into this photochemical catalysis system didn't reduce the TON, suggesting predominantly homogeneous catalysis (21, 57). In addition, isotopic labeling experiments under $^{13}CO_2$ atmosphere (58) gave a diagnostic peak of ^{13}CO in gas chromatography (GC)-mass spectrometry (MS), proving that CO was produced from the reduction of CO_2 (*SI Appendix*, Figs. S20 and S21). Furthermore, the stability test was performed by adding each component (**1**/**Pheno**/BIH) or their mixtures at 2.5 h, which indicated that catalytic deactivation resulted from the decomposition of the catalyst (**1**) and the sacrificial reductant (BIH), since the recovery of the original activity was observed by the addition of **1** and BIH to the reaction solution, while the other experiments produced much less CO (*SI Appendix*, Fig. S28).

The role of the base in photocatalysis was further investigated. The comparison experiments were performed with 0.1 M TEA/tetrabutylammonium hexafluorophosphate (TBAP) or saturated TEAB (∼0.1 M). In the photocatalysis without external water, similar performances were observed for TEA and TEAB, while the TBAP system exhibited much lower activity (*SI Appendix*, Fig. S17), suggesting the vital role of the base that accepts the proton of the one-electron-oxidation species of BIH, since TBAP is the supporting electrolyte for the electrochemical studies without basicity to accept the proton of $BIH^{\bullet+}$, and another BIH molecule may act as the base. On the other hand, negligible CO was produced in the water-containing system with TEA or TBAP (*SI Appendix*, Fig. S18), probably due to the relatively strong acidity of the conjugate acid of TEA and BIH, which may be more long-lived under the water-containing environment with higher acidity compared with the water-free system, and led to faster catalyst decomposition. For the water-containing system with TEAB, although the addition of water increased the acidity of the bulk solution and a lower TON was obtained compared with the water-free system, the conjugate acid of bicarbonate is carbonic acid, most of which would rapidly decompose into CO_2 and H_2O with much weaker acidity, and it may be the reason for the better water tolerance of the TEAB system compared with the TEA system and the TBAP system.

Quenching Mechanism of Pheno. After the characterization of **1** as an efficient catalyst for photochemical reduction of CO_2, quenching experiments were carried out to obtain further insight for the mechanism study. It should be noted that the photophysics of **Pheno** is complicated since the singlet (^{1}**Pheno***) and triplet (^{3}**Pheno***) excited states are both populated after irradiation (59, 60). Although the yield of intersystem crossing (Φ_{ISC}) from the ^{1}**Pheno*** to the ^{3}**Pheno*** excited state is as high as 91% (61), the ^{1}**Pheno*** state cannot be ignored, and the Φ_{ISC} would decrease with the addition of a suitable quencher (59). The quenching kinetics for the singlet species was studied by monitoring the shortening of the fluorescent lifetime since the ^{1}**Pheno*** state is fluorescent (59). As shown in Fig. 6A, the fluorescent lifetime remains constant with the addition of catalyst **1** among the concentration range from 0 to 0.08 mM, indicating that the oxidative quenching of

the ^{1}**Pheno*** state by the catalyst is not feasible in a typical run (0.05 mM of **1**), probably due to the short ^{1}**Pheno*** lifetime (6.9 ns; Fig. 6) and the limited concentration of **1**, although the oxidation potential from the S_1 state to the radical cation **Pheno**$^{\cdot+}$ (−1.97 V vs. NHE; *SI Appendix*, Table S4) is negative enough to drive the reduction of the catalyst (−1.37 V vs. NHE; Fig. 3). Contrarily, BIH is an efficient reductive quencher of the ^{1}**Pheno*** state, as indicated by the shortened lifetime after the addition of BIH among the concentration range from 0 to 44 mM, with a quenching rate constant (k_q) of 4.8×10^9 $M^{-1} \cdot s^{-1}$ (Fig. 6B and *SI Appendix*, Fig. S30), consistent with the more positive potential of ^{1}**Pheno***/**Pheno**$^{\cdot-}$ (0.81 V vs. NHE; *SI Appendix*, Table S4) compared with that of $BIH^{\cdot+}$/BIH (0.58 V vs. NHE; *SI Appendix*, Fig. S32).

On the other hand, transient absorption (TA) spectroscopy was investigated to shed light on the photoinduced electron transfer from ^{3}**Pheno***. Both catalyst **1** and the sacrificial donor BIH are feasible to quench ^{3}**Pheno***, with k_q values of 2.9×10^9 $M^{-1} \cdot s^{-1}$ and 9.3×10^6 $M^{-1} \cdot s^{-1}$, respectively (Fig. 7). The high k_q value for the oxidative quenching pathway is in agreement with the more negative redox potential for oxidation of ^{3}**Pheno*** (−1.61 V vs. NHE; *SI Appendix*, Table S4) compared with the reduction of **1** (−1.37 V vs. NHE; Fig. 3), while the slow kinetics for the reductive quenching pathway is probably ascribed to the low oxidation power of ^{3}**Pheno*** (0.32 V vs. NHE for ^{3}**Pheno***/**Pheno**$^{\cdot-}$; *SI Appendix*, Table S4), which is lower than the peak potential (0.58 V vs. NHE; *SI Appendix*, Fig. S32) of $BIH^{\cdot+}$/BIH, but slightly higher than the onset potential (0.30 V vs. NHE; *SI Appendix*, Fig. S32) for BIH oxidation. Nevertheless, after multiplying the rate constants by the concentrations of **1**/BIH in a typical run, the oxidative quenching rate of ^{3}**Pheno*** by **1** was calculated as 1.45×10^8 s^{-1}, while a similar value of 1.02×10^8 s^{-1} was obtained for the reductive quenching by BIH, suggesting that both of these two pathways may be feasible in a typical run. In addition, we noticed that the signal of the ground state (390 nm; Fig. 7A) failed to return to baseline within the time window with the addition of **1** (*SI Appendix*, Fig. S34), probably due to the formation of the long-lived radical cation **Pheno**$^{\cdot+}$, suggesting the oxidative quenching by the catalyst **1** rather than the energy transfer quenching (60).

Catalytic Mechanism of 1 in a Typical Run Without External Water. Fourier transform infrared spectroelectrochemistry (FTIR-SEC) was employed to obtain insight into the intermediates involved in the reaction pathway. TBAP was chosen as the electrolyte to avoid the interference of the bands of TEAB. As mentioned before, the infrared (IR) signal at 1,585 cm^{-1}, which was assigned to free acetate anion, according to the literature (62), appeared at a reductive potential under the Ar atmosphere (*SI Appendix*, Fig. S35), which was absent at a resting potential, consistent with the dissociation of the acetate anion accompanied by the reduction of the catalyst, as mentioned before for the irreversible reduction peak in Fig. 3. DFT results indicate that the departure of acetate from $Ni^I(L^-)(OAc^-)$ is exergonic, with a free-energy change of −9.0 kcal·mol^{-1}, consistent with the IR-SEC results. In addition, a similar exergonic process was also proposed in the mechanism study of **OPyNi** based on DFT calculations (13). Furthermore, the calculated structures for the related intermediates indicated that the geometry of the coordination between the carbazolide-*bis*(NHC) ligand and the nickel center doesn't change significantly. The calculated structure of **1** exhibits C1–Ni–C2 and N1–Ni–O1 angles of 161.3° and 161.0°, respectively (*SI Appendix*, Fig. S43), which are both close to the data from the single-crystal structure (*SI Appendix*, Fig. S10). A similar C1–Ni–C2 angle of 161.1° was
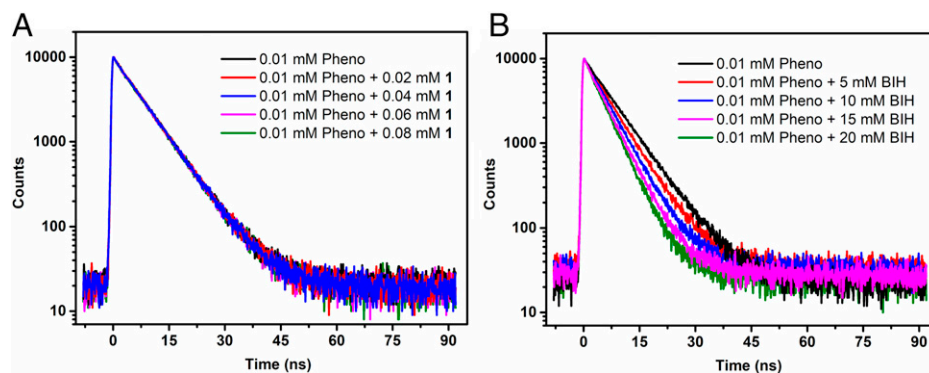
Fig. 6. Time-resolved fluorescence decay traces. (*A*) Time-resolved fluorescence decay traces at 532 nm of an acetonitrile solution containing 0.01 mM **Pheno** under N_2 in the presence of 0 to ~0.08 mM **1**. (*B*) Time-resolved fluorescence decay traces at 532 nm of a CH_3CN solution containing 0.01 mM **Pheno** under N_2 in the presence of 0 to ~20 mM BIH.

observed from the calculated structure of $Ni^I(L^-)(OAc^-)$, while the N1–Ni–O1 angle decreases to 148.7° (*SI Appendix*, Fig. S43). The Ni–O1 bond length increases to 2.15 Å in $Ni^I(L^-)(OAc^-)$ from 1.92 Å in **1** (*SI Appendix*, Fig. S43), indicating the weakened interaction between the Ni center and the acetate anion. After the departure of acetate, the $Ni^I(L^-)$ intermediate exhibits a more planar configuration with a C1–Ni–C2 angle of 174.0° (*SI Appendix*, Fig. S43). In addition, the C1–N1–C2–Ni dihedral angle of 0° indicates a planar coordination geometry in $Ni^I(L^-)$ (*SI Appendix*, Fig. S43). It should be noted that the possibility of other structural changes is not totally excluded, although some of them may be limited by the rigid structure of carbazolide, as well as the $C(sp^2)$–$N(sp^2)$ bonding between the carbazolide and the NHC fragments.

Under CO_2 atmosphere, bands at 1,681 and 1,644 cm^{-1} (Fig. 8*A*) of FTIR-SEC, corresponding to carbonate/bicarbonate, increased rapidly when the potential was scanned to the onset of the catalysis. Interestingly, two low-intense bands at ~1,966 cm^{-1} and ~2,050 cm^{-1} also concomitantly grew during the catalysis, which was assigned to the Ni^I–CO and Ni^I–CO_2 (or Ni^{II}–CO_2^-) species (Fig. 8*B*), respectively, corroborated by the DFT simulation (*SI Appendix*, Table S5). These two bands were also observed when the electrolyte was changed to TEAB, although they are not as well-defined as those in TBAP (*SI Appendix*, Fig. S36), probably due to the interference of the extremely strong IR absorption of HCO_3^-. It should be noted that the simulated wavenumber for the asymmetric C=O stretching of Ni^{II}–(CO_2^{2-}) species (1,678.8 cm^{-1}; *SI Appendix*, Table S5) is close to the carbonate/

bicarbonate bands, so it is difficult to characterize this intermediate by the FTIR-SEC method. In addition, the wavenumber for the CO vibration of Ni^{II}–CO species was calculated as 2,094 cm^{-1} (*SI Appendix*, Table S5), which was absent in the course of the reaction and is similar to the experimental value reported for an analogous nickel complex (63) (2,092.8 cm^{-1}) with a carbozolide-*bis*(NHC) ligand, suggesting the reliability of the simulation.

According to the experimental data and the literature (64, 65), a possible catalytic cycle for a typical run is proposed, as shown in Fig. 9*A*, based on the total $2e^-$-$1H^+$ transfer from BIH to CO_2 to form CO, HCO_3^- and BI^+ (1, 6, 16, 65, 66). Both of $Ni^{II}(L^-)(OAc^-)$ [**1**; L^- refers to the carbazolide-*bis*(NHC) anion ligand] and $Ni^{II}(L^-)(HCO_3^-)$ can be the initial species in the presence of bicarbonate anion, which is also one of the products of such a catalytic reaction, as indicated by the proton NMR spectroscopy (^1H NMR) of **1** with TEAB (*SI Appendix*, Fig. S37). The 1-e^- reduction of the initial species can be driven by the triplet excited state or the one-electron-reduction species of **Pheno**, given $Ni^I(L^-)$ with the departure of acetate/bicarbonate, as suggested by the irreversible cathodic wave in the CV of **1** in acetonitrile solution with TBAP (Fig. 3) or TEAB (*SI Appendix*, Fig. S38), as well as the FTIR-SEC (*SI Appendix*, Fig. S35) results. The CO_2 molecule was proposed to be activated by the $Ni^I(L^-)$ in accordance with the signal of CO_2-activated species observed in FTIR-SEC experiments (Fig. 8), as well as the significantly enhanced current density at this reduction potential in CV under CO_2 atmosphere compared with that under Ar (Fig. 3 and *SI Appendix*, Fig. S38). In addition, the normalized current
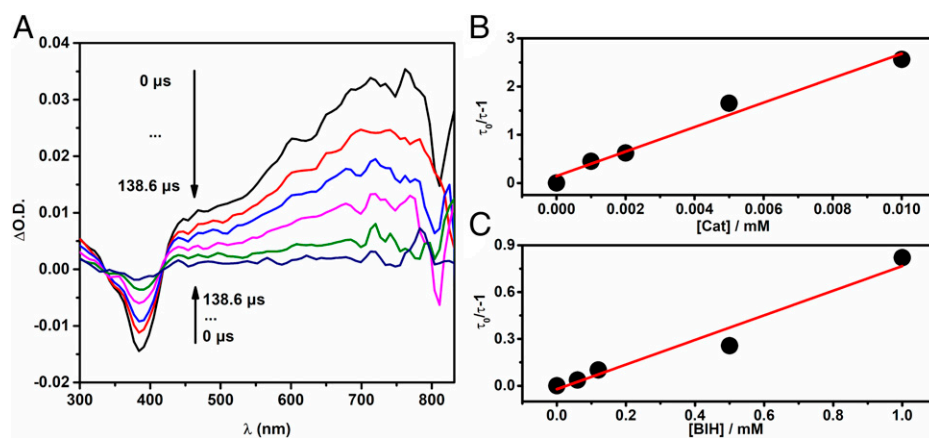

Fig. 7. TA spectroscopy. (*A*) TA spectra of 5 μM **Pheno**. (*B*) Plots of ($\tau_0/\tau - 1$) vs. the concentration of the catalyst with linear fitting. (*C*) Plots of ($\tau_0/\tau - 1$) vs. the concentration of BIH with linear fitting. The data were collected in CH_3CN under N_2 atmosphere upon excitation at 410 nm and probed at 660 nm. O.D., optical density.

density at this wave by the square root of the scan rate decreased with the increasing scan rate, which is also consistent with a chemical step, such as CO_2 coordination (*SI Appendix*, Figs. S39 and S40). Then, the second electron transfer and C–O cleavage assisted by another CO_2 molecule and/or a proton give the CO product. Since the IR signal of Ni^{II}–CO species is absent in the FTIR-SEC experiments (Fig. 8*A* and *SI Appendix*, Table S5), the regenerated Ni^{II} species is more likely to be $Ni^{II}(L^-)(HCO_3^-)$ after the release of CO, which is also consistent with the lower free energy of $Ni^{II}(L^-)(HCO_3^-)$ relative to that of $Ni^{II}(L^-)(CO)$, as indicated by the DFT result that the latter one owns a higher free energy by 0.6 kcal·mol^{-1} and the significantly higher concentration of bicarbonate anion in contrast with the dissolved CO concentration in MeCN. It should be noted that the $Ni^I(L^-)$ formed by the first reduction step would combine with a CO molecule to generate $Ni^I(L^-)(CO)$, along with the continuous production of CO, as indicated by the FTIR-SEC results (Fig. 8).

In the proposed catalytic cycle, two chemical steps, the CO_2 activation step and the C–O cleavage step, were further investigated by DFT calculations. The results show that the latter one is more likely to be the rate-determining step with calculated transition-state free energy of 25.0 or 22.7 kcal·mol^{-1}, while the barrier for CO_2 activation is only 7.0 kcal·mol^{-1}, taking $Ni^I(L^-)$ as the zero-energy point (*SI Appendix*, Fig. S44). If the free energy of $Ni^I(L^-)(CO)$ is set as zero, the barrier for CO_2 activation is 11.8 kcal·mol^{-1}. For the C–O cleavage step, two possible pathways, the protonation-first pathway (*SI Appendix*, Fig. S45) and the cleavage-first pathway (Fig. 9*B*), were considered in the calculations at first. In the cleavage-first pathway, both the structures of singlet and triplet $Ni^{II}(L^-)(COO^{2-})$ species were evaluated. There are two conformations (**S1** and **S1′**) for the closed-shell singlet species. The square-planar **S1′** shows higher free energy of 4.3 kcal·mol^{-1} than the distorted-square-planar **S1** (*SI Appendix*, Fig. S54), consistent with the crystal structure of **1** (47). The C–O cleavage takes place after the combination of $Ni^{II}(L^-)(COO^{2-})$ species and another molecule of CO_2, probably via the triplet pathway with an activation free energy of 14.3 kcal·mol^{-1}, which is much lower than that for the singlet pathway (24.7 kcal·mol^{-1}). This result can be ascribed to the significant penalty of ligand-field distortion for the singlet species, whose electron structure changes from a distorted square-planar ligand field to a distorted tetragonal-pyramidal ligand field (67), where the antibonding dz^2 is occupied (*SI Appendix*, Figs. S46 and S53). In the triplet transition-state structure, **TS$_T$**, one apical site and one equatorial site are occupied by one C atom and one O atom, respectively, suggesting the advantage of a pincer ligand (*SI Appendix*, Fig. S46). The relative free energy of the transition state for the triplet cleavage-first pathway is 25.0 kcal·mol^{-1}, which is lower than that for the protonation-first pathway (28.9 kcal·mol^{-1}; *SI Appendix*, Fig. S45). In order to further investigate the C–O cleavage mechanism, ^{13}C NMR spectroscopy (^{13}C NMR) was applied to detect the possible carbonate/bicarbonate by-product (*SI Appendix*, Fig. S41). The photochemical reaction was performed under $^{13}CO_2$, and TEAB was replaced by TEA to avoid the isotope exchange. The ^{13}C NMR signals at 158.3 parts per million (ppm) and 156.4 ppm after irradiation can be assigned to $H^{13}CO_3^-$ and $^{13}CO_3^{2-}$, while negligible related signal was observed for the mixture without irradiation, indicating that the involvement of the second CO_2 in the C–O cleavage step may be possible, according to the literature (68, 69). It should be noted that direct C–OH cleavage may occur without the assistance of the second CO_2 molecule. Although we failed to locate the corresponding singlet transition state, probably due to the instable pentacoordinate singlet Ni^{II} structure, the triplet transition state **TS$_{S3}$** was located successfully with a relative free energy of 22.7 kcal·mol^{-1} (*SI Appendix*, Figs. S45 and S48), which is slightly lower than that for the cleavage-first pathway. However, this energy might be underestimated due to the low concentration of water, which provides proton to form the $Ni^{II}(L^-)$–COOH species during the catalysis in a typical run without the addition of water. Therefore, both the cleavage-first pathway and the direct C–OH cleavage pathway might be possible. Besides these three pathways based on the $2e^- -1H^+$ reduction, the possibility of a proton-assisted C–O cleavage cannot be totally excluded during the catalysis, as the accumulation of protons may occur, which will be discussed in detail later, although this $2e^- -2H^+$ mechanism is not consistent with the $2e^- -1H^+$ oxidation of BIH, and the ^{13}C NMR signal of HCO_3^- and CO_3^{2-} (*SI Appendix*, Fig. S41) were observed after the photocatalysis with $^{13}CO_2$ and TEA (without TEAB), indicating the possibility of C–O cleavage assisted by the second CO_2 molecule.

Origin of the One-Stone-Two-Birds Effect. The one-stone-two-birds strategy plays a vital role in the observed excellent
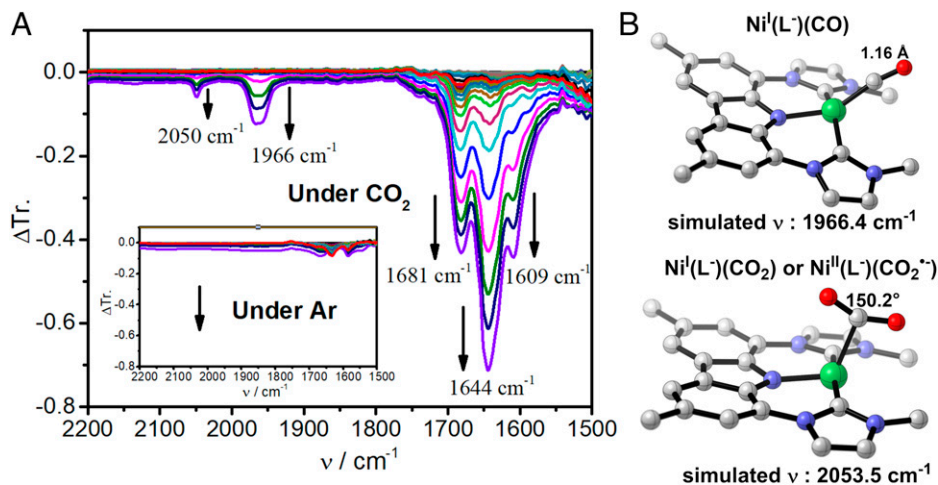

Fig. 8. Reaction intermediates. (*A*) Differential FTIR-SEC spectra during the negative scan of **1** in acetonitrile solution with 0.1 M TBAP under CO_2 atmosphere (*Inset* shows the spectra under Ar atmosphere). (*B*) The calculated structures of $Ni^I(L^-)(CO)$ and $Ni^I(L^-)(CO_2)/Ni^{II}(L^-)(CO_2^{\cdot-})$, which are proposed to be corresponding to the band at ∼1,966 cm^{-1} and ∼2,050 cm^{-1} in *A*, respectively. Hydrogen atoms of C–H bonds are omitted for clarity. L^- refers to the carbazolide-*bis*(NHC) anion ligand. Atom color: Ni, green; C, gray; N, blue; O, red.

catalytic performance. The extended-conjugating carbazolide-based ligand can serve as an electron-transfer mediator to stabilize the highly reduced triplet intermediates. As shown in Fig. 10A, the spin density of the carbazolide-*bis*(NHC) ligand in **T1** [triplet state of $Ni^{II}(L^-)(CO_2^{2-})$; Fig. 9B] is 0.620, which is higher than that in the corresponding intermediate of the pyridinol-*bis*(NHC) complex (^{OPy}**T1**; 0.470). Therefore, the free-energy change from **S1** to **T1** (Fig. 9B) is lower than that for a similar transformation from ^{OPy}**S1** to ^{OPy}**T1** (*SI Appendix*, Fig. S55). Additionally, thanks to the strongly electron-donating carbazolide site, **T1** exhibits strong back-π-donation from the three-dimensional (3D) electrons of the Ni center to the π* orbital of the CO_2 moiety, which benefits the C–O cleavage. Charge decomposition analysis (CDA; Fig. 10B) (70, 71) indicates that the value for the total donation from Ni to CO_2 moiety in **T1** (0.114) is comparable to that in ^{OPy}**T1** (0.104), which also bears a strongly electron-donating ligand. For the reason above, the carbazolide-based complex **1** with one-stone-two-birds effect, exhibits lower free energy of the transition states for the rate-limiting C–O cleavage step compared with the pyridinol-based complex **OPyNi** [25.0 kcal·mol^{-1} vs. 28.4 kcal·mol^{-1} for the cleavage-first pathway and 22.7 kcal·mol^{-1} vs. 29.7 kcal·mol^{-1} for the direct C–OH cleavage pathway, relative to the singlet $Ni^{II}(CO_2^{2-})$ species; Fig. 9B and *SI Appendix*, Figs. S45, S46, S48, S55, and S56].

Catalytic Mechanism of 1 with External Water. In a water-containing system, a $2e^- - 2H^+$ reduction of CO_2 may be preferred for the introduction of an external proton source (35). After the generation of $Ni^{II}(L^-)(COOH^-)$ by the first protonation step, C–OH cleavage could take place assisted by Brønsted acid. Although a high barrier of 32.0 kcal·mol^{-1} was calculated for this step assisted by (CO_2+H_2O) (*SI Appendix*, Fig. S49, relative to **S4**), we obtained a much lower barrier of 4.5 kcal·mol^{-1} when the Brønsted acid was changed to H_2CO_3 (*SI Appendix*, Fig. S50, relative to **S4**), consistent with the higher TOF of the water-containing system, highlighting the important role of external Brønsted acid (35).

Discussion

In conclusion, a combined strategy with appending both π-conjugation and electron-donating moieties has been successfully applied by using a large π-conjugating and strong electron-donating carbazolide fragment as the middle coordination site to design a pincer *bis*-NHC nickel catalyst, leading to significantly improved performance for selective photochemical catalytic reduction of CO_2. The catalytic mechanism was investigated by complementary experimental methods and computational studies, highlighting the vital roles of the extended conjugation and electron-donor character of the carbazolide fragment. Moreover, a
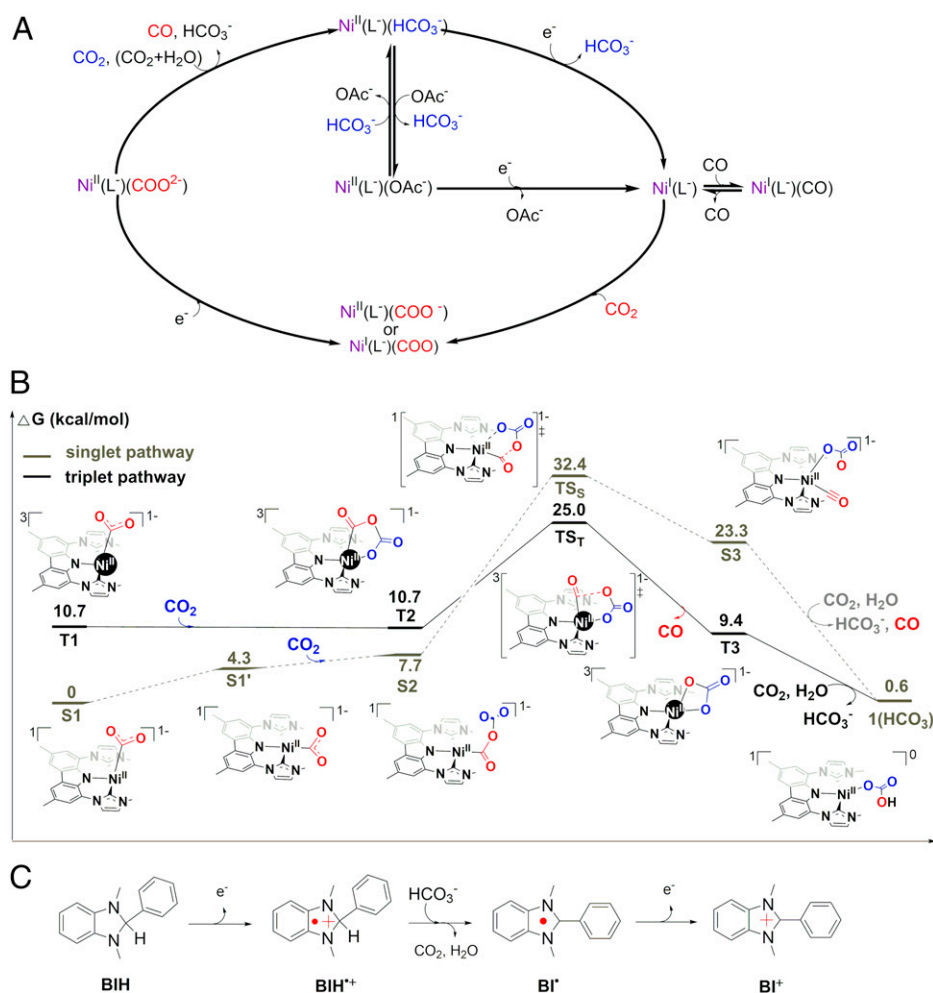

Fig. 9. Catalytic mechanism. (A) Proposed mechanism for CO_2 reduction by catalyst **1** in a typical run. L^- refers to the carbazolide-*bis*(NHC) anion ligand. (B) Free-energy profiles of the singlet/triplet C–O cleavage pathway (cleavage-first) of **1** at the B3LYP-D3 (73, 74)/def2TZVP(SMD)//B3LYP-D3/def2SVP level of theory. Spin multiplicities and charges of the intermediates are presented at the upper left and the upper right of the corresponding structures, respectively. (C) The proposed $2e^- - 1H^+$ oxidation of BIH in a typical run (66).
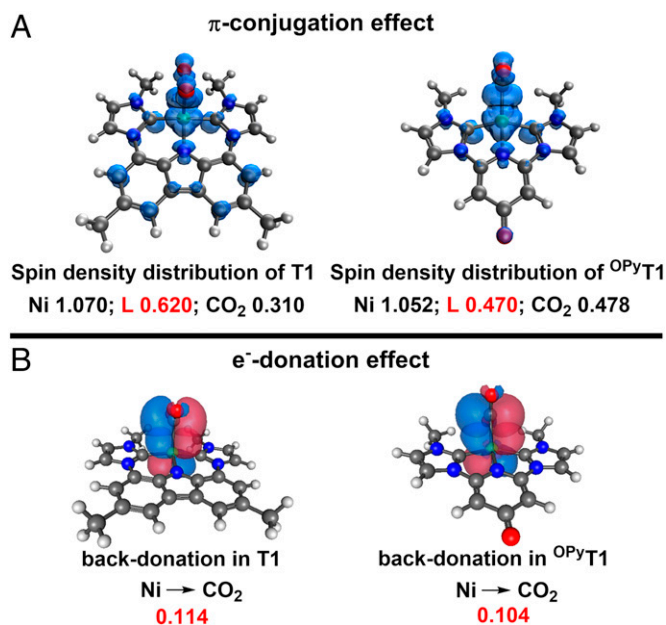
A π-conjugation effect

Spin density distribution of T1
Ni 1.070; L 0.620; CO₂ 0.310

Spin density distribution of ᴼᴾʸT1
Ni 1.052; L 0.470; CO₂ 0.478

B e⁻-donation effect

back-donation in T1
Ni → CO₂
0.114

back-donation in ᴼᴾʸT1
Ni → CO₂
0.104

Fig. 10. Origin of the one-stone-two-birds effect. (*A*) Spin-density distributions of **T1** and the corresponding intermediate of **OPyNi** (ᴼᴾʸ**T1**). (*B*) Back-π-donation from the 3D electrons of Ni to the π* orbital of CO₂ moiety in **T1** and ᴼᴾʸ**T1**. The CDA values for the total donation from Ni to CO₂ moieties are shown in red. Atom color: Ni, green; C, gray; N, blue; O, red.

high quantum efficiency of 11.2% was obtained of the nickel complex with a cheap organic PS. The results provide a potential strategy toward the development of efficient and applicable photocatalysts for selective CO_2 reduction to CO.

Materials and Methods

Materials. Catalyst **1** was synthesized and characterized by a literature method (47). MeCN (99.9%, extra dry, with molecular sieves; water ≤ 10 ppm [by Karl Fischer], EnergySeal) was purchased from Energy Chemical Co. Ltd. All other chemicals were commercially available and used without further purification. The purity of both argon and CO_2 was 99.999%.

Instruments. Mass spectra were obtained by using a Thermo Finnigan LCQ DECA XP ion-trap mass spectrometer. UV-vis spectra were determined on a Shimadzu UV-3150 spectrophotometer. The irradiation experiments were conducted with LED light (Zolix, MLED4; λ = 450/425 nm) or a 300-W Xe lamp (PerfectLight, FLS-FX300HU) equipped with an AM 1.5 filter. Electrochemical measurements were carried out by using an electrochemical workstation CHI 620E. Pt wire was used as a counterelectrode in the three-electrode system. For CV measurement, the reference electrode and the working electrode were 0.1 M Ag/AgNO₃ electrode and glassy carbon electrode, respectively. The potential of 0.1 M Ag/AgNO₃ reference electrode was calibrated by using ferrocene/ferrocenium (Fc⁰/⁺) as an external standard. The generated gas samples were analyzed by a Shimadzu Instruments GC-2014C gas chromatograph with a thermal conductivity detector and two flame-ionization detectors. The liquid phase of the reaction system was analyzed by ion chromatography (Metrohm, 930 Compact IC Flex, Supp 5 anion column, Na₂CO₃/NaHCO₃ aqueous eluent) to detect the presence of formate. SEC experiments were carried out by using an optically transparent thin-layer electrode cell and a Bruker Optics VERTEX 70/70V series FT-IR spectrometer. The fluorescent lifetime measurements and quenching experiments were conducted on a modular fluorescent life and steady-state fluorescence spectrometer (FLSP980, Edinburgh Instruments LTD.). Nanosecond TA spectra were measured on the LP980 laser flash photolysis instrument (Edinburgh) at λ_pump = 410 nm. The gas products of isotopic labeling experiments under ¹³CO₂ atmosphere were analyzed by GC-MS (Agilent 7890A-5975C, column: GS-CarbonPLOT).

Photochemical Experiments.

1. For the test using Ir(ppy)₃ as PS with LED light, the photocatalytic reduction of CO_2 to CO was conducted under 1 atm of a certain atmosphere (CO_2 or Ar) at room temperature in a 16-mL reactor containing catalyst, Ir(ppy)₃ (0.1 mM), BIH (11 mM), TEA (0.25 mL), and 5 mL of MeCN, unless otherwise stated. The reaction mixture was continuously stirred with a magnetic bar and irradiated under blue LED light (λ = 450 nm, ~100 mW·cm⁻²). The generated gases were analyzed by GC, and the products in the solution, if produced, were analyzed by ion chromatography. No formate was detected in the liquid phase.

2. For the test using **Pheno** as PS, the photocatalytic reduction of CO_2 to CO was conducted under 1 atm of a certain atmosphere (CO_2 or Ar) at room temperature in a 16-mL reactor containing catalyst, **Pheno** (0.1 mM), BIH (11 mM), saturated TEAB, and 3 mL of MeCN, unless otherwise stated. The reaction mixture was continuously stirred with a magnetic bar and irradiated under an LED light (λ = 425 nm, ~100 mW·cm⁻² or 1.78 mW·cm⁻²), unless otherwise stated. The generated gases were analyzed by GC, and the products in the solution, if produced, were analyzed by ion chromatography. No formate was detected in the liquid phase.

3. For the comparison between **1** and **OPyNi**, the reaction conditions were set according to the literature (13). The solution was irradiated with a solar-simulated spectrum set to 1 Sun (300 W Xe lamp, AM 1.5 filter). Other conditions were 0.1 mM catalyst, 0.1 mM Ir(ppy)₃, 11 mM BIH, 0.25 mL of TEA, 1 atm of CO_2, and 5 mL of MeCN.

Quantum Yield Determination. The total number of incident photons was measured by using an optical power meter (Coherent LabMax-TOP) at room temperature. The photon flux of 425-nm LED light (1.78 mW·cm⁻²) was determined to be 1.39×10^{-8} einstein/s. Quantum yield was calculated according to the following equation:

$$\Phi_{CO} = [(\text{number of the produced molecule})/(\text{number of photons})] \times 100\%.$$

Reaction conditions were: **1** (0.05 mM), **Pheno** (0.1 mM), BIH (11 mM), and saturated TEAB with 60 μL of water in 3 mL of CO_2-saturated MeCN solution.

Data, Materials, and Software Availability. All study data are included in the article and/or *SI Appendix*.

Author affiliations: ᵃSchool of Materials Science and Engineering, Sun Yat-sen University, Guangzhou 510275, People's Republic of China; ᵇKey Laboratory for Polymeric Composite & Functional Materials of Ministry of Education, School of Chemistry, Sun Yat-sen University, Guangzhou 510275, People's Republic of China; and ᶜInstitute for New Energy Materials and Low Carbon Technologies, School of Materials Science and Engineering, Tianjin University of Technology, Tianjin 300384, People's Republic of China

1. Y. Yamazaki, H. Takeda, O. Ishitani, Photocatalytic reduction of CO_2 using metal complexes. *J. Photoch. Photobio. C* **25**, 106–137 (2015).
2. J.-W. Wang, W.-J. Liu, D.-C. Zhong, T.-B. Lu, Nickel complexes as molecular catalysts for water splitting and CO_2 reduction. *Coord. Chem. Rev.* **378**, 237–261 (2019).
3. K. Elouarzaki, V. Kannan, V. Jose, H. S. Sabharwal, J. M. Lee, Recent trends, benchmarking, and challenges of electrochemical reduction of CO_2 by molecular catalysts. *Adv. Energy Mater.* **9**, 1900090 (2019).
4. T. W. Schneider, M. T. Hren, M. Z. Ertem, A. M. Angeles-Boza, [Ruᴵᴵ(tpy)(bpy)Cl]⁺-Catalyzed reduction of carbon dioxide. Mechanistic insights by carbon-13 kinetic isotope effects. *Chem. Commun. (Camb.)* **54**, 8518–8521 (2018).
5. C. M. Boudreaux et al., Ruthenium(ii) complexes of pyridinol and N-heterocyclic carbene derived pincers as robust catalysts for selective carbon dioxide reduction. *Chem. Commun. (Camb.)* **53**, 11217–11220 (2017).
6. Y. Tamaki, K. Koike, O. Ishitani, Highly efficient, selective, and durable photocatalytic system for CO_2 reduction to formic acid. *Chem. Sci. (Camb.)* **6**, 7213–7221 (2015).

7. T. Morimoto et al., Ring-shaped Re(I) multinuclear complexes with unique photofunctional properties. *J. Am. Chem. Soc.* **135**, 13266–13269 (2013).

8. T. W. Schneider, M. Z. Ertem, J. T. Muckerman, A. M. Angeles-Boza, Mechanism of photocatalytic reduction of CO_2 by Re(bpy)(CO)$_3$Cl from differences in carbon isotope discrimination. *ACS Catal.* **6**, 5473–5481 (2016).

9. S. Sung, D. Kumar, M. Gil-Sepulcre, M. Nippe, Electrocatalytic CO_2 reduction by imidazolium-functionalized molecular catalysts. *J. Am. Chem. Soc.* **139**, 13993–13996 (2017).

10. N. P. Liyanage et al., Photochemical CO_2 reduction with mononuclear and dinuclear rhenium catalysts bearing a pendant anthracene chromophore. *Chem. Commun. (Camb.)* **55**, 993–996 (2019).

11. P. Lang et al., Sensitized photochemical CO_2 reduction by hetero-pacman compounds linking a Re^I tricarbonyl with a porphyrin unit. *Chemistry* **25**, 4509–4519 (2019).

12. P. Lang, R. Giereth, S. Tschierlei, M. Schwalbe, Unexpected wavelength dependency of the photocatalytic CO_2 reduction performance of the well-known (bpy)Re(CO)$_3$Cl complex. *Chem. Commun. (Camb.)* **55**, 600–603 (2019).

13. D. B. Burks et al., Nickel(ii) pincer complexes demonstrate that the remote substituent controls catalytic carbon dioxide reduction. *Chem. Commun. (Camb.)* **54**, 3819–3822 (2018).

14. T. Ouyang, H.-H. Huang, J.-W. Wang, D.-C. Zhong, T.-B. Lu, A dinuclear cobalt cryptate as a homogeneous photocatalyst for highly selective and efficient visible-light driven CO_2 reduction to CO in CH$_3$ CN/H$_2$O solution. *Angew. Chem. Int. Ed. Engl.* **56**, 738–743 (2017).

15. J.-W. Wang, L. Jiang, H.-H. Huang, Z. Han, G. Ouyang, Rapid electron transfer via dynamic coordinative interaction boosts quantum efficiency for photocatalytic CO_2 reduction. *Nat. Commun.* **12**, 4276 (2021).

16. H. Takeda et al., Highly efficient and robust photocatalytic systems for CO_2 reduction consisting of a Cu(I) photosensitizer and Mn(I) catalysts. *J. Am. Chem. Soc.* **140**, 17241–17254 (2018).

17. H. Takeda, K. Ohashi, A. Sekine, O. Ishitani, Photocatalytic CO_2 reduction using Cu(I) photosensitizers with a Fe(II) catalyst. *J. Am. Chem. Soc.* **138**, 4354–4357 (2016).

18. A. Rosas-Hernández, C. Steinlechner, H. Junge, M. Beller, Earth-abundant photocatalytic systems for the visible-light-driven reduction of CO_2 to CO. *Green Chem.* **19**, 2356–2360 (2017).

19. H. Yuan, B. Cheng, J. Lei, L. Jiang, Z. Han, Promoting photocatalytic CO_2 reduction with a molecular copper purpurin chromophore. *Nat. Commun.* **12**, 1835 (2021).

20. J. Bonin, M. Robert, M. Routier, Selective and efficient photocatalytic CO_2 reduction to CO using visible light and an iron-based homogeneous catalyst. *J. Am. Chem. Soc.* **136**, 16768–16771 (2014).

21. Z. Guo et al., Highly efficient and selective photocatalytic CO_2 reduction by iron and cobalt quaterpyridine complexes. *J. Am. Chem. Soc.* **138**, 9413–9416 (2016).

22. Y. Wang, X.-W. Gao, J. Li, D. Chao, Merging an organic TADF photosensitizer and a simple terpyridine-Fe(iii) complex for photocatalytic CO_2 reduction. *Chem. Commun. (Camb.)* **56**, 12170–12173 (2020).

23. H. Rao, C.-H. Lim, J. Bonin, G. M. Miyake, M. Robert, Visible-light-driven conversion of CO_2 to CH$_4$ with an organic sensitizer and an iron porphyrin catalyst. *J. Am. Chem. Soc.* **140**, 17830–17834 (2018).

24. Y. Wang, T. Liu, L. Chen, D. Chao, Water-assisted highly efficient photocatalytic reduction of CO_2 to CO with noble metal-free bis(terpyridine)iron(II) complexes and an organic photosensitizer. *Inorg. Chem.* **60**, 5590–5597 (2021).

25. Y. Wang, L. Chen, T. Liu, D. Chao, Coordination-driven discrete metallo-supramolecular assembly for rapid and selective photocatalytic CO_2 reduction in aqueous solution. *Dalton Trans.* **50**, 6273–6280 (2021).

26. L. Chen et al., A molecular noble metal-free system for efficient visible light-driven reduction of CO_2 to CO. *Dalton Trans.* **48**, 9596–9602 (2019).

27. H. Rao, J. Bonin, M. Robert, Visible-light homogeneous photocatalytic conversion of CO_2 into CO in aqueous solutions with an iron catalyst. *ChemSusChem* **10**, 4447–4450 (2017).

28. S. E. Lee et al., Visible-light photocatalytic conversion of carbon dioxide by Ni(II) complexes with N$_4$S$_2$ coordination: Highly efficient and selective production of formate. *J. Am. Chem. Soc.* **142**, 19142–19149 (2020).

29. T.-Y. Shang et al., Recent advances of 1,2,3,5-tetrakis(carbazol-9-yl)-4,6-dicyanobenzene (4CzIPN) in photocatalytic transformations. *Chem. Commun. (Camb.)* **55**, 5408–5419 (2019).

30. H. Wang et al., Electronic modulation of non-van der Waals 2D electrocatalysts for efficient energy conversion. *Adv. Mater.* **33**, e2008422 (2021).

31. H. Wang et al., Transition metal nitrides for electrochemical energy applications. *Chem. Soc. Rev.* **50**, 1354–1390 (2021).

32. P. Prabhu, J.-M. Lee, Metallenes as functional materials in electrocatalysis. *Chem. Soc. Rev.* **50**, 6700–6719 (2021).

33. P. Prabhu, V. Jose, J.-M. Lee, Design strategies for development of TMD-based heterostructures in electrochemical energy systems. *Matter* **2**, 526–553 (2020).

34. P. Prabhu, V. Jose, J.-M. Lee, Heterostructured catalysts for electrocatalytic and photocatalytic carbon dioxide reduction. *Adv. Funct. Mater.* **30**, 1910768 (2020).

35. K. T. Ngo et al., Turning on the protonation-first pathway for electrocatalytic CO_2 reduction by manganese bipyridyl tricarbonyl complexes. *J. Am. Chem. Soc.* **139**, 2604–2618 (2017).

36. S. Gonell, J. Lloret-Fillol, A. J. M. Miller, An iron pyridyl-carbene electrocatalyst for low overpotential CO_2 reduction to CO. *ACS Catal.* **11**, 615–626 (2021).

37. F. Franco, M. F. Pinto, B. Royo, J. Lloret-Fillol, A highly active n-heterocyclic carbene manganese(I) complex for selective electrocatalytic CO_2 reduction to CO. *Angew. Chem. Int. Ed. Engl.* **57**, 4603–4606 (2018).

38. S. Gonell et al., The trans effect in electrocatalytic CO_2 reduction: Mechanistic studies of asymmetric ruthenium pyridyl-carbene catalysts. *J. Am. Chem. Soc.* **141**, 6658–6671 (2019).

39. S. Gonell, E. A. Assaf, K. D. Duffee, C. K. Schauer, A. J. M. Miller, Kinetics of the *trans* effect in ruthenium complexes provide insight into the factors that control activity and stability in CO_2 electroreduction. *J. Am. Chem. Soc.* **142**, 8980–8999 (2020).

40. V. S. Thoi, N. Kornienko, C. G. Margarit, P. Yang, C. J. Chang, Visible-light photoredox catalysis: Selective reduction of carbon dioxide to carbon monoxide by a nickel N-heterocyclic carbene-isoquinoline complex. *J. Am. Chem. Soc.* **135**, 14413–14424 (2013).

41. X. Su, K. M. McCardle, J. A. Panetier, J. W. Jurss, Electrocatalytic CO_2 reduction with nickel complexes supported by tunable bipyridyl-N-heterocyclic carbene donors: Understanding redox-active macrocycles. *Chem. Commun. (Camb.)* **54**, 3351–3354 (2018).

42. J. D. B. Koenig, J. Willkomm, R. Roesler, W. E. Piers, G. C. Welch, Electrocatalytic CO_2 reduction at lower overpotentials using iron(III) tetra(meso-thienyl)porphyrins. *ACS Appl. Energy Mater.* **2**, 4022–4026 (2019).

43. C. Yang et al., Stable luminescent iridium(iii) complexes with bis(N-heterocyclic carbene) ligands: Photo-stability, excited state properties, visible-light-driven radical cyclization and CO_2 reduction, and cellular imaging. *Chem. Sci. (Camb.)* **7**, 3123–3136 (2016).

44. D. Bézier, C. Guan, K. Krogh-Jespersen, A. S. Goldman, M. Brookhart, Experimental and computational study of alkane dehydrogenation catalyzed by a carbazolide-based rhodium PNP pincer complex. *Chem. Sci. (Camb.)* **7**, 2579–2586 (2016).

45. J. Higuchi et al., Preparation and reactivity of iron complexes bearing anionic carbazole-based PNP-type pincer ligands toward catalytic nitrogen fixation. *Dalton Trans.* **47**, 1117–1121 (2018).

46. C. Cheng et al., Synthesis and characterization of carbazolide-based iridium PNP pincer complexes. Mechanistic and computational investigation of alkene hydrogenation: Evidence for an Ir(III)/Ir(V)/Ir(III) catalytic cycle. *J. Am. Chem. Soc.* **136**, 6672–6683 (2014).

47. T.-Y. Lee et al., Nickel-catalyzed coupling of carbon dioxide with cyclohexene oxide by well-characterized bis(n-heterocyclic carbene) carbazolide complexes. *Organomet.* **36**, 291–297 (2017).

48. J. D. Cope et al., Electrocatalytic reduction of CO_2 with CCC-NHC pincer nickel complexes. *Chem. Commun. (Camb.)* **53**, 9442–9445 (2017).

49. M. Sheng et al., A nickel complex with a biscarbene pincer-type ligand shows high electrocatalytic reduction of CO_2 over H$_2$O. *Dalton Trans.* **44**, 16247–16250 (2015).

50. H. Shirley et al., Durable solar-powered systems with Ni-catalysts for conversion of CO_2 or CO to CH$_4$. *J. Am. Chem. Soc.* **141**, 6617–6622 (2019).

51. T. B. Donadt, A. M. Lilio, T. A. Stinson, B. Lama, O. R. Luca, DOSY NMR and normal pulse voltammetry for the expeditious determination of number of electrons exchanged in redox events. *ChemistrySelect* **3**, 7410–7415 (2018).

52. A. J. Huckaba, E. A. Sharpe, J. H. Delcamp, Photocatalytic reduction of CO_2 with re-pyridyl-NHCs. *Inorg. Chem.* **55**, 682–690 (2016).

53. Z. Guo et al., Selectivity control of CO versus HCOO$^-$ production in the visible-light-driven catalytic reduction of CO_2 with two cooperative metal sites. *Nat. Catal.* **2**, 801–808 (2019).

54. B. G. McCarthy et al., Structure-property relationships for tailoring phenoxazines as reducing photoredox catalysts. *J. Am. Chem. Soc.* **140**, 5088–5101 (2018).

55. Y. Du et al., Strongly reducing, visible-light organic photoredox catalysts as sustainable alternatives to precious metals. *Chemistry* **23**, 10962–10968 (2017).

56. R. M. Pearson, C.-H. Lim, B. G. McCarthy, C. B. Musgrave, G. M. Miyake, Organocatalyzed atom transfer radical polymerization using N-aryl phenoxazines as photoredox catalysts. *J. Am. Chem. Soc.* **138**, 11399–11407 (2016).

57. L. Chen et al., Molecular catalysis of the electrochemical and photochemical reduction of CO_2 with earth-abundant metal complexes. Selective production of CO vs HCOOH by switching of the metal center. *J. Am. Chem. Soc.* **137**, 10918–10921 (2015).

58. D. Hong et al., Efficient photocatalytic CO_2 reduction by a Ni(II) complex having pyridine pendants through capturing a Mg^{2+} ion as a Lewis-acid cocatalyst. *J. Am. Chem. Soc.* **141**, 20309–20317 (2019).

59. Y. M. Lattke et al., Interrogation of O-ATRP activation conducted by singlet and triplet excited states of phenoxazine photocatalysts. *J. Phys. Chem. A* **125**, 3109–3121 (2021).

60. M. Kudisch, C.-H. Lim, P. Thordarson, G. M. Miyake, Energy transfer to Ni-amine complexes in dual catalytic, light-driven C-N cross-coupling reactions. *J. Am. Chem. Soc.* **141**, 19479–19486 (2019).

61. S. M. Sartor, B. G. McCarthy, R. M. Pearson, G. M. Miyake, N. H. Damrauer, Exploiting charge-transfer states for maximizing intersystem crossing yields in organic photoredox catalysts. *J. Am. Chem. Soc.* **140**, 4778–4781 (2018).

62. P. Di Bernardo et al., Energetics and structure of uranium(VI)-acetate complexes in dimethyl sulfoxide. *Inorg. Chem.* **51**, 9045–9055 (2012).

63. D. C. Marelius et al., Hydrogen-bonding pincer complexes with two protic N-heterocyclic carbenes from direct metalation of a 1,8-bis(imidazol-1-yl)carbazole by platinum, palladium, and nickel. *Chemistry* **21**, 10988–10992 (2015).

64. X. Chai et al., Highly efficient and selective photocatalytic CO_2 to CO conversion in aqueous solution. *Chem. Commun. (Camb.)* **56**, 3851–3854 (2020).

65. H. Takeda, C. Cometto, O. Ishitani, M. Robert, Electrons, photons, protons and earth-abundant metal complexes for molecular catalysis of CO_2 reduction. *ACS Catal.* **7**, 70–88 (2017).

66. Y. Tamaki, K. Koike, T. Morimoto, O. Ishitani, Substantial improvement in the efficiency and durability of a photocatalyst for carbon dioxide reduction using a benzoimidazole derivative as an electron donor. *J. Catal.* **304**, 22–28 (2013).

67. C. Hou et al., Unusual non-bifunctional mechanism for Co-PNP complex catalyzed transfer hydrogenation governed by the electronic configuration of metal center. *Dalton Trans.* **44**, 16573–16585 (2015).

68. S. Das et al., Highly active ruthenium CNC pincer photocatalysts for visible-light-driven carbon dioxide reduction. *Inorg. Chem.* **58**, 8012–8020 (2019).

69. R. R. Rodrigues, C. M. Boudreaux, E. T. Papish, J. H. Delcamp, Photocatalytic reduction of CO_2 to CO and formate: Do reaction conditions or ruthenium catalysts control product selectivity? *ACS Appl. Energy Mater.* **2**, 37–46 (2019).

70. T. Lu, F. Chen, Multiwfn: A multifunctional wavefunction analyzer. *J. Comput. Chem.* **33**, 580–592 (2012).

71. X. Meng, L. Tian, Generalized charge decomposition analysis (GCDA) method. *J. Adv. Phys. Chem.* **4**, 111–124 (2015).

72. Y. Zhao, D. G. Truhlar, The M06 suite of density functionals for main group thermochemistry, thermochemical kinetics, noncovalent interactions, excited states, and transition elements: Two new functionals and systematic testing of four M06-class functionals and 12 other functionals. *Theor. Chem. Acc.* **120**, 215–241 (2008).

73. A. D. Becke, Density-functional thermochemistry. III. The role of exact exchange. *J. Chem. Phys.* **98**, 5648–5652 (1993).

74. S. Grimme, J. Antony, S. Ehrlich, H. Krieg, A consistent and accurate ab initio parametrization of density functional dispersion correction (DFT-D) for the 94 elements H-Pu. *J. Chem. Phys.* **132**, 154104 (2010).